

Review

Study on Dislocation-Dopant Ions Interaction in Ionic Crystals by the Strain-Rate Cycling Test during the Blaha Effect

Yohichi Kohzuki

Department of Mechanical Engineering, Saitama Institute of Technology, Saitama 369-0293, Japan; kohzuki@sit.ac.jp

Received: 23 October 2017; Accepted: 8 January 2018; Published: 12 January 2018

Abstract: The interaction between a dislocation and impurities has been investigated by measurements of yield stress and proof stress, micro-hardness tests, direct observations of dislocation, internal friction measurements, or stress relaxation tests so far. A large number of investigations has been carried out by the separation of the flow stress into effective and internal stresses on the basis of the temperature dependence of yield stress, the strain rate dependence of flow stress, and stress relaxation. Nevertheless, it is difficult to investigate the interaction between a dislocation and obstacles during plastic deformation by the mentioned methods. As for the original method which combines strain-rate cycling tests with the Blaha effect measurement, the original method is different from above-mentioned ones and would be possible to clear it up. The strain-rate cycling test during the Blaha effect measurement has successively provided the information on the dislocation motion breaking away from the strain fields around dopant ions with the help of thermal activation, and seems to separate the contributions arising from the interaction between dislocation and the point defects and those from dislocations themselves during plastic deformation of ionic crystals. Such information on dislocation motion in bulk material cannot be obtained by the widely known methods so far. Furthermore, the various deformation characteristics derived from the original method are sensitive to a change in the state of dopant ions in a specimen by heat treatment, e.g., the Gibbs free energy (G_0) for overcoming of the strain field around the dopant by a dislocation at absolute zero becomes small for the annealed KCl:Sr²⁺ single crystal ($G_0 = 0.26$ eV) in comparison with that for the quenched one ($G_0 = 0.39$ eV).

Keywords: ultrasonic oscillatory stress; strain-rate sensitivity of flow stress; activation energy for dislocation motion; forest dislocation density; heat treatment

1. Introduction

The interaction between a dislocation and point defects has been investigated by measurements of yield stress (e.g., [1–7]) and proof stress (e.g., [8,9]), micro-hardness tests (e.g., [10–14]), direct observations of dislocation (e.g., [15–21]), internal friction measurements (e.g., [22–27]), or stress relaxation tests (e.g., [28,29]) so far. A large number of investigations have been carried out by the separation of the flow stress into effective and internal stresses on the basis of the temperature dependence of yield stress, the strain rate dependence of flow stress, and the stress relaxation. Nevertheless, it is difficult to investigate the interaction between a dislocation and obstacles during plastic deformation by the mentioned methods. This is because yield stress depends on dislocation velocity, dislocation density, and multiplication of dislocations [30] and proof stress is used as a means of assessing the yield stress. On the other hand, the effect of heat treatment on the micro-hardness is almost insensitive to the change of atomic order of point defects in a specimen. As for direct observations, electron microscopy provides the information on the interaction between a dislocation

and obstacles for a thin specimen but not for bulk, and also light scattering method is useful only for a transparent specimen. X-ray topography is the lack of resolution in the photograph, so that the specimen is limited to the low dislocation density below 10^4 cm^{-2} . Internal friction measurements cannot provide the information on the motion of the dislocation which moves by overcoming the forest dislocations and the weak obstacles such as impurities during plastic deformation, because the measurements concern the motion of the dislocation which breaks away from the weak obstacles between two forest dislocations by vibration [31]. In stress relaxation tests it is generally assumed that internal structure of crystals does not change, i.e., dislocation density and internal stress are constant. In this paper, the study on interaction between a dislocation and dopant ions is made by the strain-rate cycling tests during the Blaha effect measurement.

The Blaha effect is the phenomenon that static flow stress decreases when an ultrasonic oscillatory stress is superimposed [32]. Blaha and Langenecker found it when the ultrasonic oscillatory stress of 800 kHz was superimposed during plastic deformation of Zn single crystals. Figure 1 shows the variation of the stress-strain curve by superimposed ultrasonic vibrations as an example of their experimental results [20]. The curve represents the intermittent addition of ultrasonic vibrations in a solid line and the continued addition in a broken line. This phenomenon is the so-called the Blaha effect. The same phenomena have been confirmed in many metals (e.g., [33–35]) and have been widely made to apply to the plastic working technique for industrial purpose such as wire drawing, deep drawing, rolling, and another metal forming techniques, since this phenomenon has an industrial significance (e.g., [36–44]). The Blaha effect has been explained by a temperature rise of materials [45], an abrupt increase in mobile dislocation density [46], a reduction in internal stress [47–49], or a stress superposition mechanism [50–55] so far. The temperature rise is not so high as to influence the flow stress in this test (the strain-rate cycling test during the Blaha effect measurement). It is also improbable that the mobile dislocation density markedly increases immediately after the application of oscillations. If the Blaha effect is explained by itself, the mobile dislocation density has to increase by a factor of tens or hundreds. The reduction in internal stress should be valid only for the particular case that the amplitude of oscillatory stress is so large as to change the internal structure, where a redistribution of the dislocations may occur. The stress superposition mechanism, where the internal friction due to application of oscillations is neglected and the amplitude dependent region (Q_H^{-1}) of internal friction is not considered, has been regarded as the most important one to interpret the Blaha effect. However, Lebedev et al. [49,56] reported that the stress decrement ($\Delta\tau$) due to the application of ultrasonic oscillatory stress appears at the moment when measurements of the amplitude dependence of internal friction were made. Ohgaku and Takeuchi [57] also concluded that $\Delta\tau$ is proportional to Q_H^{-1} at small amplitude for NaCl and KCl single crystals. The relation between $\ln\Delta\tau$ and $\ln Q_H^{-1}$ is shown in Figure 2, which is drawn from the experimental results for single crystals of KCl, NaCl, NaBr, and KBr. The relation is divided into three regions denoted by I, II, and III. It was furthermore found that the average length of dislocation segments become long when the internal friction measurement was carried out [58]. Therefore, it could be considered that $\Delta\tau$ of alkali halide is attributed to the increase in activation volume for dislocation motion when dislocations move with the aid of thermal activation [57,59]. Assuming that the mobile dislocation density and the enthalpy at zero effective stress keep constant before and after application of oscillatory stress, this can be interpreted on the basis of the following discussion. The activation volume (V_0) and the effective stress (τ_e) will change into V and τ , respectively, when an oscillation is applied. Then, we can obtain

$$V_0\tau_e = V\tau \quad (1)$$

because the strain rate keeps constant before and after application of oscillations. Equation (1) directly gives

$$\Delta\tau = \tau_e - \tau = \left(1 - \frac{V_0}{V}\right)\tau_e \quad (2)$$

Accordingly, the increment in activation volume, namely the increment in the average length of dislocation segments (ΔL) as given by Equation (3), causes $\Delta\tau$ of alkali halide.

$$\Delta V = b\Delta Ld \quad (3)$$

where b is the magnitude of Burgers vector and d is the activation distance.

The $\Delta\tau$ increases with increasing stress amplitude and slightly increases with strain rate ($\dot{\epsilon}$) [59]. The strain rate dependence of the $\Delta\tau$ may suggest that the stress change ($\Delta\tau'$) due to the strain-rate cycling depend on the stress amplitude and on the $\Delta\tau$. Then, Ohgaku and Takeuchi [59] carried out the strain-rate cycling tests under superposition of an oscillatory stress.

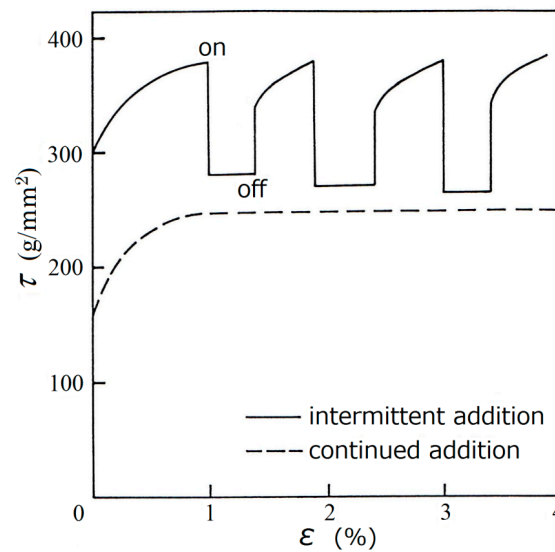


Figure 1. Variation of the stress-strain curve for Zn single crystals by superimposed ultrasonic vibrations (reproduced from reference [32] with permission from the publisher).

The strain-rate cycling test during the Blaha effect measurement is illustrated in Figure 3. The stress drop $\Delta\tau$ is caused by superposition of oscillatory stress (τ_v) during plastic deformation. When strain-rate cycling between the strain rates of $\dot{\epsilon}_1$ and $\dot{\epsilon}_2$ is carried out keeping the stress amplitude of τ_v constant, the stress change due to the strain-rate cycling is $\Delta\tau'$. Figure 4 shows the result at room temperature for single crystals of nominally pure alkali halide such as NaCl, KCl, NaBr, and KBr. The relative curve between $\Delta\tau'$ and $\Delta\tau$ shifts upward with strain and bends at a critical $\Delta\tau$. The critical $\Delta\tau$ corresponds to the point which separates region I and region II in Figure 2. They identified the small $\Delta\tau$ region in Figure 4 with region I in Figure 2 and the larger $\Delta\tau$ region with regions II and III. The relations between $\Delta\tau$ and Q_H^{-1} as well as $\Delta\tau$ and $\Delta\tau'$ are essentially divided into two regions, where different mechanisms are considered to dominate. In region III, it concerns the dislocation density, because Q_H^{-1} linearly decreases as applied shear stress, which is generally proportional to the square root of the dislocation density [60–62], becomes large in region III [63]. When the tests are carried out, $\Delta\tau'$ can be expressed by

$$\Delta\tau' = \Delta\tau'_i + \Delta\tau'_p + \Delta\tau'_s \quad (4)$$

where the suffixes of stress variation, i, p, and s, mean the internal stress, the part of the effective stress due to impurities, and the strain-dependent part of the effective stress, respectively. They considered Figure 4 on the basis of Equation (4) as follows. $\Delta\tau'_p$ corresponds to the linearly decreasing part of $\Delta\tau'$ at small stress amplitude in Figure 4 and is given by the difference between $\Delta\tau'$ at $\Delta\tau$ of zero and $\Delta\tau'$ at the critical point which distinguishes regions I and II. $\Delta\tau'_s$ dominates in regions II and III,

where $\Delta\tau'_p$ is zero. $\Delta\tau'_s$ increases with increasing strain and dislocation density. Li reported that the effective internal stress depends on the flow stress [64]. When a dislocation velocity-stress exponent is nearly 30 and the maximum internal stress is close to the flow stress, the effective internal stress approaches the maximum internal stress [64]. With regard to $\Delta\tau'_i$, it was considered by the results in the paper [64] that the influence of internal stress during the strain-rate cycling under the oscillation is negligible. This can be examined also from the experimental result in Section 3.4 (i.e., λ_p is almost constant independently of the strain). Therefore, the strain-rate cycling tests during the Blaha effect measurement seems to separate the contributions arising from the interaction between a dislocation and dopant ions and those from dislocations themselves during plastic deformation.

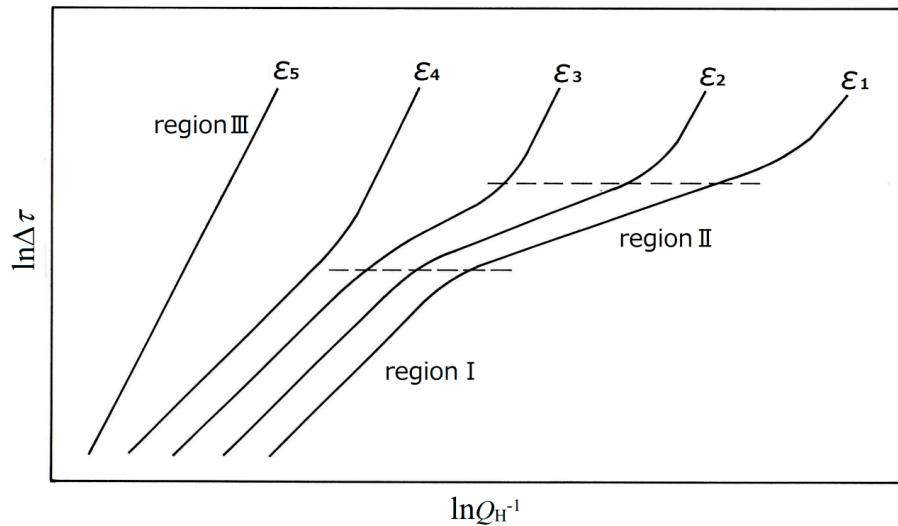


Figure 2. Schematic relation between $\ln\Delta\tau$ and $\ln Q_H^{-1}$ (reproduced from reference [63] with permission from the publisher). The strain, ε , increases with its suffix.

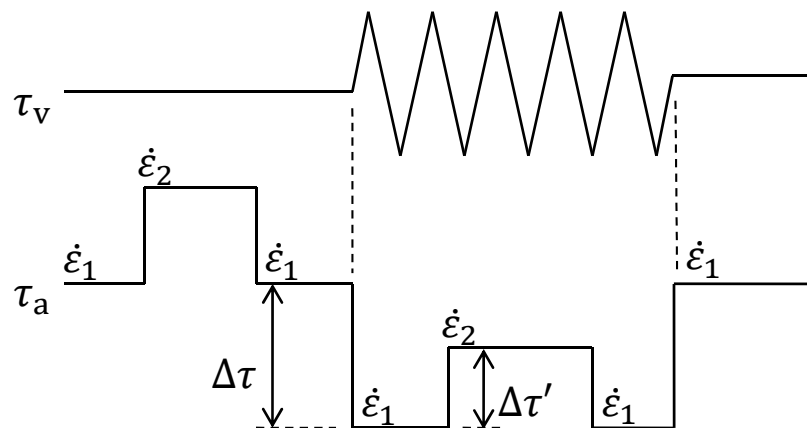


Figure 3. Variation of applied shear stress, τ_a , when the strain-rate cycling between the strain rates, $\dot{\varepsilon}_1$ ($2.2 \times 10^{-5} \text{ s}^{-1}$) and $\dot{\varepsilon}_2$ ($1.1 \times 10^{-4} \text{ s}^{-1}$), is carried out under superposition of ultrasonic oscillatory shear stress, τ_v .

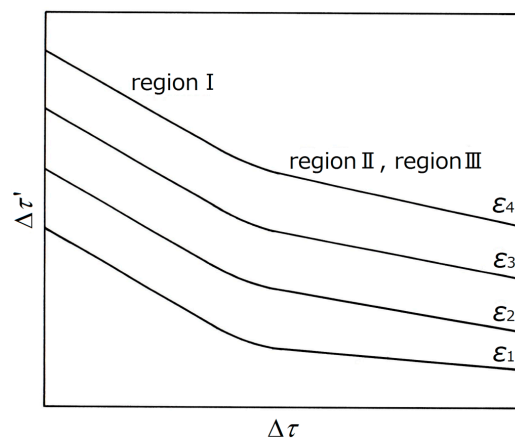


Figure 4. Schematic relation between $\Delta\tau'$ and $\Delta\tau$ at room temperature (reproduced from reference [63] with permission from the publisher). The strain increases with its suffix.

Ohgaku and Takeuchi [57,63] reported that the strain-rate cycling tests associated with the ultrasonic oscillation can separate the contributions arising from the interaction between a dislocation and dopant ions and from the dislocations themselves during plastic deformation at room temperature. Then, they discussed the temperature dependence of the effective stress due to monovalent dopants (i.e., Br^- or I^-) in $\text{KCl}:\text{Br}^-$ (0.5, 1.0, and 2.0 mol.% in the melt) or I^- (0.2, 0.5, and 1.0 mol.% in the melt) single crystals at 77 to 420 K [65] and $\text{NaCl}:\text{Br}^-$ (0.1, 0.5, and 1.0 mol.% in the melt) single crystals at 77 to 253 K [66]. They found that the measurement of strain-rate sensitivity under the application of ultrasonic oscillatory stress provides useful information on the interaction between a mobile dislocation and the dopant ions [65,66]. It has been reported so far through the combination method that the information on the dislocation motion can be obtained in terms of various ionic crystals. The details are reviewed mainly for $\text{KCl}:\text{Sr}^{2+}$ single crystals.

As compared with metals, the ionic crystals used here have some advantages: A small number of glide systems, low dislocation density in grown crystal (e.g., 10^4 cm^{-2} order for NaCl single crystal [67]) as against that of annealed metals (e.g., 1 to $5 \times 10^6 \text{ cm}^{-2}$ in pure Cu single crystal [68] and 10^7 cm^{-2} order for pure Fe single crystal [69]), transparency and readiness for single crystal preparation, etc. Pure or impurity-doped alkali halide crystals, therefore, are excellent materials for an investigation on mechanical properties of crystals. A large number of investigations on strength of materials have been made with alkali halide crystals (e.g., [19,70,71]).

2. Experimental Procedure

2.1. Preparation of Specimens

Two kinds of single crystals used in this work, nominally pure KCl , KCl doped with SrCl_2 (0.035, 0.050, 0.065 mol.% in melt) were grown from the melt of reagent-grade powders by the Kyropoulos method in air. The specimens, which were prepared by cleaving out of single crystalline ingots to the size of $5 \times 5 \times 15 \text{ mm}^3$, were kept immediately below the melting point for 24 h in order to reduce dislocation density as much as possible, followed by cooling to room temperature at the rate of 40 K h^{-1} . This is termed the specimen A. The additive Sr^{2+} ions are supposed to aggregate owing to the gradual cooling in the specimen A. Accordingly, the specimens A were held at 673 K for 30 min, followed by quenching to room temperature immediately before the test, in order to disperse the additive Sr^{2+} ions into them. The temperature (i.e., 673 K) of this heat treatment was determined on the basis of the below experimental results.

Figure 5 shows the dependence of initial dislocation density (ρ), the dielectric loss peak due to the I-V pairs ($\tan\delta$), and yield stress (τ_y) on the temperature from which $\text{KCl}:\text{Sr}^{2+}$ (0.3 and 1.0 mol.% in the melt) single crystals were quenched [72]. Etch pits technique was used to detect the density of

dislocations in $\text{KCl}:\text{Sr}^{2+}$ (0.3 mol.% in the melt) with a corrosive liquid (saturated solution of PbCl_2 + ethyl alcohol added two drops of water). The etching was carried out at room temperature for 30 min. The dielectric loss factor $\tan\delta$ as a function of frequency was measured for $\text{KCl}:\text{Sr}^{2+}$ (1.0 mol.% in the melt) in thermostatic bath within 300 to 873 K. The height of the loss peak is related to the concentration of isolated I-V dipole (see Equation (7)). The τ_y values were obtained at room temperature for $\text{KCl}:\text{Sr}^{2+}$ (1.0 mol.% in the melt) compressed along the $\langle 100 \rangle$ axis at the crosshead speed of $20 \mu\text{m min}^{-1}$. As a result, it was found that the dislocation density and the yield stress remarkably increase for the crystals quenched from the temperature (T) above 673 K. While the value of $\tan\delta$ does not vary by quenching from the temperature below 573 K or above 673 K. In Figure 5, the values of ρ , $\tan\delta$, and τ_y at about 300 K correspond to the specimen A and those at 673 K the specimen A quenched from 673 K. When alkali halide crystals are doped with divalent cations, the dopant cations induce positive ion vacancies in order to conserve the electrical neutrality and are expected to be paired with the vacancies. They are often at the nearest neighbor sites forming a divalent impurity-vacancy (I-V) dipole, which attract them strongly [73], for crystals quenched from a high temperature. Then asymmetrical distortions (tetragonal lattice distortions) are produced around the I-V dipoles. Mobile dislocations on a slip plane interact strongly only with these defects lying within one atom spacing of the glide plane [74]. The concentration of isolated I-V dipoles affects the yield stress, as reported in the papers [75–78]. The difference in dislocation density is slight and the $\tan\delta$ obviously becomes larger with higher quenching temperature between 573 and 673 K as shown in Figure 5. Therefore, the specimens are determined to be quenched from 673 K to room temperature immediately before the compression tests mentioned below.

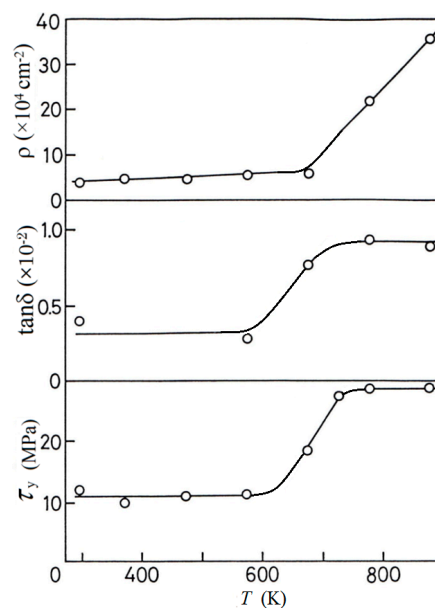
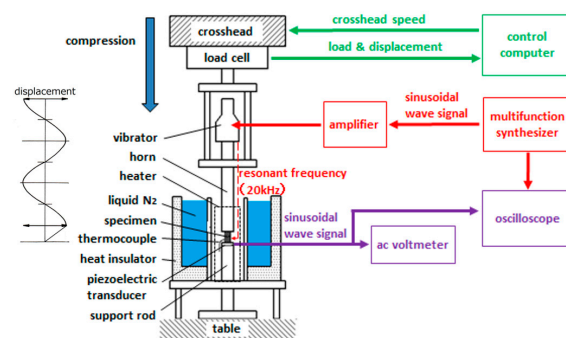


Figure 5. Dependence of initial dislocation density (ρ), the dielectric loss peaks due to the I-V pairs ($\tan\delta$), and yield stress (τ_y) on the quenching temperature (reproduced from reference [72]).

2.2. Strain-Rate Cycling Test during the Blaha Effect

The schematic illustration of apparatus is shown in Figure 6a. A resonator composed of a vibrator and a horn was attached to an Instron-type testing machine DSS-500 (Shimadzu Corp., Kyoto, Japan), in Figure 6b. The specimens, of which the upper and bottom sides were coated with molybdenum disulfide as a lubricant to prevent from barrel shape deformation during the test, were lightly fixed on a piezoelectric transducer and then cooled down to a test temperature. The specimens were deformed by compression along the $\langle 100 \rangle$ axis, and the ultrasonic oscillatory stress with the signal of 20 kHz from a multifunction synthesizer was intermittently superimposed for one or two minutes by the resonator

in the same direction as the compression. The amplitude of the oscillatory stress was monitored by the output voltage from the piezoelectric transducer set on the bottom side of specimen (i.e., between a specimen and the support rod), which was observed by an a.c. voltmeter or an oscilloscope. The strain of the specimen is considered to be homogeneous, because the wavelength, which is 196 mm by calculating from the data of reference [79], is 13 times as long as the length of the specimen. Strain-rate cycling test during the Blaha effect measurement was already illustrated in Figure 3. Superposition of oscillatory stress (τ_v) during plastic deformation causes a stress drop (as $\Delta\tau$, in MPa). Keeping the stress amplitude of τ_v constant, strain-rate cycling between the strain rates of $\dot{\epsilon}_1$ ($2.2 \times 10^{-5} \text{ s}^{-1}$) and $\dot{\epsilon}_2$ ($1.1 \times 10^{-4} \text{ s}^{-1}$) was carried out. Then, the stress change due to the strain-rate cycling is $\Delta\tau'$. Slip system for rock-salt structure such as KCl crystal is $\{110\} \langle 1\bar{1}0 \rangle$ so that shear stress (τ) and shear strain (ϵ) calculated for the slip system were used in this study. The strain-rate cycling tests made between the crosshead speeds of 20 and $100 \mu\text{m min}^{-1}$ were performed at 77 K up to the room temperature as shown in Figure 6c. For the tests at 77 K, the specimen was immersed in the liquid nitrogen. The other temperature measurements were made by heater controlled using thermocouples of Ni-55%Cu vs. Cu, in Figure 6d. Each specimen was held at the test temperature for 30 min prior to the compression test, and the stability of temperature during the test was kept within 2 K. The strain-rate sensitivity ($\Delta\tau'/\Delta\ln\dot{\epsilon}$) of the flow stress, which is given by $\Delta\tau'/1.609$, was used as a measurement of the strain-rate sensitivity (as $\lambda = \Delta\tau'/\Delta\ln\dot{\epsilon}$, in MPa).



(a)



Figure 6. Experimental apparatus: (a) Schematic block diagram of apparatus system; (b) main testing machine; (c) resonator connected with the test machine and heat-insulator box; (d) heater covered specimen in the heat-insulator box.

3. Results and Discussion

3.1. Relations between $\Delta\tau$ and Strain-Rate Sensitivity (λ) for KCl:Sr²⁺ and KCl

The variation of λ with shear strain is shown in Figure 7a for KCl:Sr²⁺ (0.050 mol.%) single crystal at 200 K. Figure 7b concerns $\Delta\tau$ for the same specimen. $\Delta\tau$ does not largely change with shear strain and is almost constant independently of the strain. This means that the process of plastic deformation does not affect the decrease of flow stress due to superposition of oscillatory stress. However, $\Delta\tau$ increases with increasing stress amplitude at a given temperature and shear strain. λ tends to increase with shear strain at all stress amplitude (except for $\tau_v = 45$ below the strain of about 9%) and decrease with stress amplitude at a given shear strain. The increase of λ with shear strain is caused by the increase of the forest dislocation density. The value of $(\Delta\lambda/\Delta\tau_v)_{T,\epsilon}$ seems to be small at low and high stress amplitude as can be seen in Figure 7a. The values of $\Delta\tau$ and λ , which is obtained from Figure 7 at the shear strains of 10%, 14% and 18%, are plotted in Figure 8. The figure provides the relationship between $\Delta\tau$ and λ for a fixed internal structure of the KCl:Sr²⁺ (0.050 mol.%) single crystal at 200 K. As can be seen from Figure 8, the variation of λ with $\Delta\tau$ has stair-like shape. That is to say, there are two bending points on the each curve, and there are two plateau regions: The first plateau region ranges below the first bending point at low $\Delta\tau$ and the second one extends from the second bending point at high $\Delta\tau$. The second plateau place is considered to correspond to the regions II and III in Figure 4, as reported by Ohgaku and Takeuchi [63]. The λ gradually decreases with $\Delta\tau$ between the two bending points. λ_p denoted in Figure 8 is introduced later (Section 3.4). The values of $\Delta\tau$ at the first and the second bending points are referred to as τ_{p1} and τ_{p2} in MPa, respectively. However, no first bending point (i.e., τ_{p1}) is on the relative curve of $\Delta\tau$ and λ for nominally pure KCl single crystal. This is revealed in Figure 9 represented the relationship of $\Delta\tau$ and λ for the KCl at several temperatures. As for KCl, the first plateau region does not appear on each curve and λ decreases with increasing $\Delta\tau$ at low stress decrement. In contrast to KCl:Sr²⁺ single crystals, there is only one bending point on each curve, which is considered to correspond to τ_{p2} . Therefore, τ_{p1} is due to the additive ions (Sr²⁺) in the crystals. Figure 8 shows also the influence of shear strain on the relation between $\Delta\tau$ and λ . The curve shifts upwards with increasing shear strain. This phenomenon is caused by the part of the strain-rate sensitivity which depends on dislocation cuttings as well as KCl. Since the dislocation cuttings increase with increasing strain, the λ increases [63]. Stair-like relation curve of $\Delta\tau$ vs. λ is obtained for KCl:Sr²⁺ at any other temperature. Figure 10 shows the influence of temperature on the $\Delta\tau$ vs. λ curve for the crystal at strain 10%, which is obtained by the above-mentioned method. Similar result as Figure 8 is also obtained at low temperature. As the temperature is higher, τ_{p1} and τ_{p2} tend to be lower, and τ_{p1} disappears at 225 K. If τ_{p1} is the effective stress due to the weak obstacles (i.e., the additive Sr²⁺ ions) on the mobile dislocation during plastic deformation of KCl:Sr²⁺ single crystals, it should depend on temperature and Sr²⁺ concentration. Figure 11a–c shows the dependence of τ_{p1} , τ_{p2} , and yield stress τ_y on temperature for KCl:Sr²⁺ (0.065, 0.050, and 0.035 mol.%, respectively) single crystals, where the curves for these stresses are to guide the reader's eye. It is clear from the figure that τ_{p1} and τ_{p2} tend to increase with decreasing temperature as the variation of τ_y in the temperature range applied for the three specimens. Both τ_{p1} and τ_{p2} seem to depend on Sr²⁺ concentration at a given temperature. τ_{p1} may increase with the solute concentration (c_0) as below

$$\tau_{p1} = \sqrt{\frac{F^3 c_0}{2\mu b^6}} \quad (5)$$

where F is the force acted on the dislocation and μ is the shear modulus. Equation (5) is derived from the Friedel relation [80] between the effective stress and the average length of dislocation segments. Figure 12 shows the dependence of τ_{p1} and τ_{p2} on the yield stress for KCl:Sr²⁺ at 150 K. The plots correspond to the case when the Sr²⁺ concentration is 0.035, 0.050, and 0.065 mol.% from the bottom. It can be seen from this figure that both τ_{p1} and τ_{p2} are approximately proportional to the yield stress.

This means that τ_{p1} and τ_{p2} increase, depending on the Sr^{2+} concentration, because the yield stress generally increases with increasing impurity concentration [1–3,75,81].

The critical temperature (T_c), at which the T - τ_{p1} curves intersect the abscissa and τ_{p1} is zero, may be determined from Figure 11. Then, T_c appears to be constant independently of the Sr^{2+} concentration and τ_y seems to approach a constant value above the T_c .

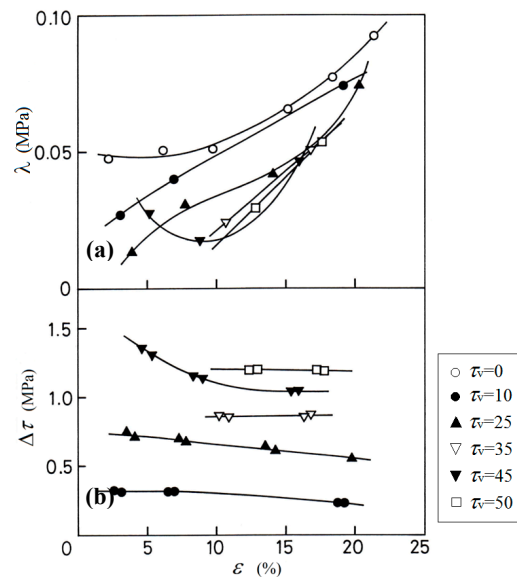


Figure 7. Variation of (a) the strain-rate sensitivity, λ ($= \Delta\tau' / \Delta \ln \dot{\varepsilon}$) of flow stress, and (b) the stress decrement, $\Delta\tau$, due to the superimposition of ultrasonic oscillation with shear strain at 200 K and various stress amplitude for KCl:Sr²⁺ (0.050 mol.%) single crystal (reproduced from reference [82] with permission from the publisher). τ_v (arb. units): (○) 0, (●) 10, (▲) 25, (▽) 35, (▼) 45, and (□) 50. The ultrasonic oscillatory stress (τ_v) increases with its numbers besides each symbol.

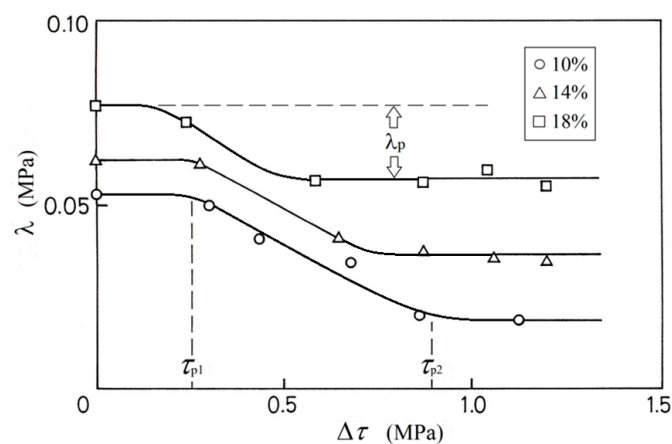


Figure 8. Relation between the strain-rate sensitivity and the stress decrement for KCl:Sr²⁺ (0.050 mol.%) at 200 K (reproduced from reference [82] with permission from the publisher). ε : (○) 10%, (△) 14%, and (□) 18%. The plotted points are obtained from Figure 7a,b.

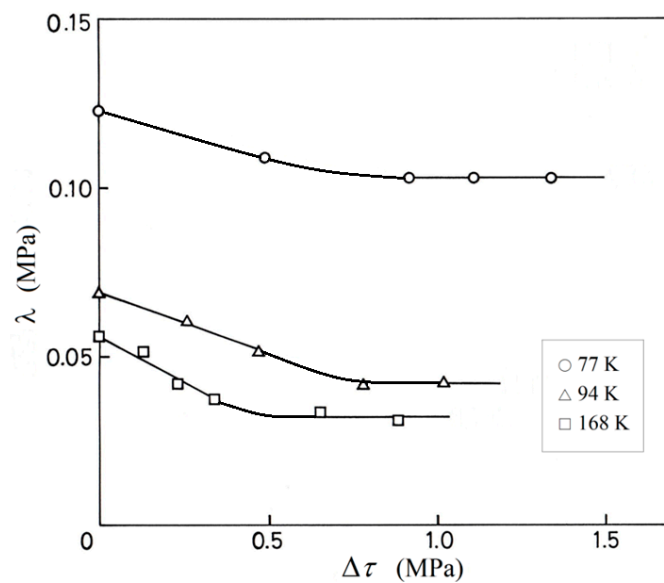


Figure 9. Relation between the strain-rate sensitivity and the stress decrement for KCl at various temperatures: (○) 77 K, (△) 94 K, (□) 168 K (reproduced from reference [82] with permission from the publisher).

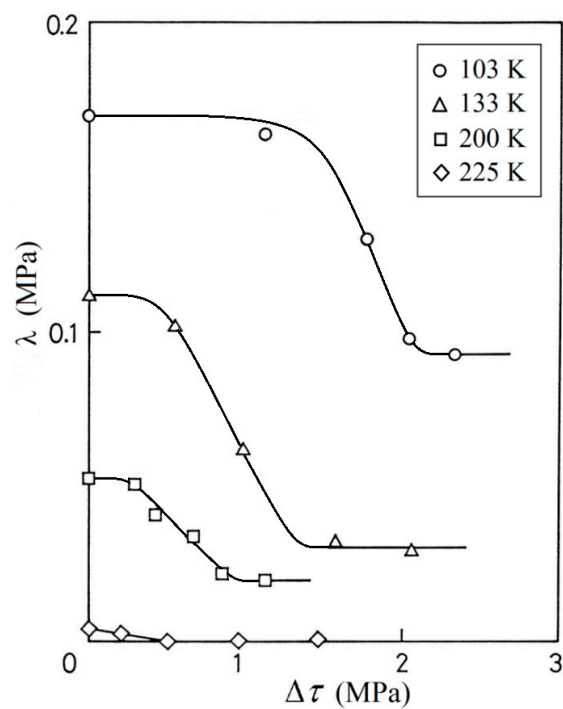


Figure 10. Relation between the strain-rate sensitivity and the stress decrement at the shear strain of 10 % for KCl:Sr²⁺ (0.050 mol.%) at various temperatures: (○) 103 K, (△) 133 K, (□) 200 K, (◇) 225 K (reproduced from reference [83] with permission from the publisher).

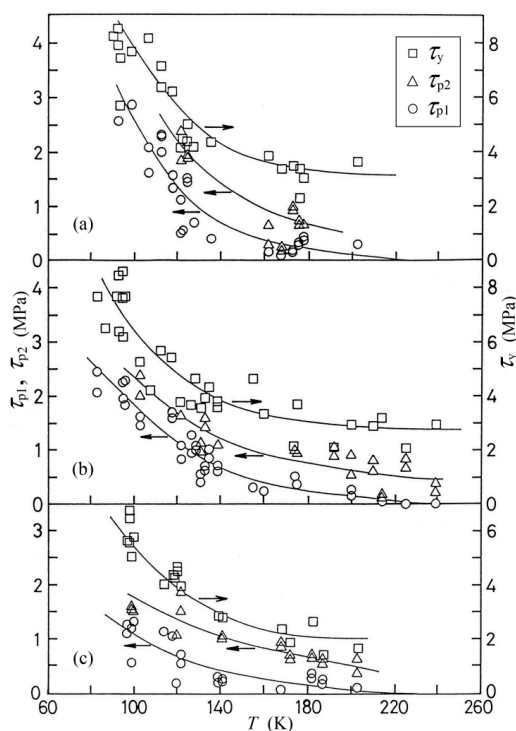


Figure 11. Dependence of (○) τ_{p1} , (△) τ_{p2} , and (□) τ_y on temperature for KCl:Sr²⁺. Sr²⁺ concentration is (a) 0.065, (b) 0.050, and (c) 0.035 mol.%.

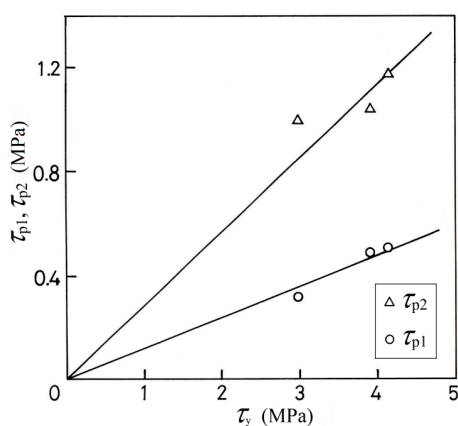


Figure 12. Dependence of (○) τ_{p1} and (△) τ_{p2} on the yield stress, τ_y , for KCl:Sr²⁺ at 150 K (reproduced from reference [82] with permission from the publisher). Concentration of Sr²⁺ is 0.035, 0.050, 0.065 mol.% from the left.

3.2. Discussion for the $\Delta\tau$ vs. λ Curve

The preceding experimental facts that the $\Delta\tau$ vs. λ curve for KCl:Sr²⁺ has two bending points and two plateau regions, and both τ_{p1} and τ_{p2} depend on Sr²⁺ concentration, suggest that the phenomena shown in Figures 8 and 10 are attributable to the interaction between a dislocation and only one type of obstacle. The reason for this is discussed below.

The strain-rate sensitivity of effective stress (τ^*) is inversely proportional to the activation volume, i.e., the average length of dislocation segment, as given by

$$\left(\frac{\Delta\tau^*}{\Delta\ln\dot{\epsilon}}\right)_T = \frac{kT}{V}, (V = bLd) \quad (6)$$

where k is the Boltzmann constant. In addition, it is reported that the length of the dislocation segment increases and the strain-rate sensitivity decreases when the ultrasonic oscillatory stress is applied at room temperature during plastic deformation and that the plateau region is due to the dislocation cuttings when oscillations cause the dislocation to break away from all weak obstacles [84]. Therefore, the first plateau region, as well as the second one, indicates that the average length of the dislocation segments remains constant there. In other words, application of oscillations with low stress amplitude cannot influence the average length of the dislocation segments at low temperature, but it can do so at high temperature, such as room temperature. Therefore, the plateau region appears at low stress decrement in Figures 8 and 10. Now it is imaged that a dislocation is pinned by many weak obstacles and is bowing by applied stress between a few strong obstacles such as forest dislocations during stationary plastic deformation. When the stress amplitude increases, the dislocation begins to break away from weak obstacles by oscillation between the strong ones and the average length of the dislocation begins to increase. The λ starts to decrease at the stress decrement of τ_{p1} . This τ_{p1} should depend on temperature and on density of the obstacle. τ_{p1} is considered to represent the effective stress due to the weak obstacles which lie on the dislocation when the dislocation begins to break away from these weak obstacles with the help of oscillation. Observation of τ_{p1} , therefore, provides information on the interaction between a dislocation and weak obstacles. Consequently, the phenomena shown in Figures 8–10 seem to reflect the influence of ultrasonic oscillation on the dislocation motion on the slip plane containing many weak obstacles and a few strong ones, during plastic deformation. The weak obstacles are considered to be the dopant ions and not to be vacancies here, because the vacancies in the specimen have low density in contrast to the dopants. For example, the concentration of vacancies at thermal equilibrium state is about 1.2×10^{-7} % for KCl single crystal quenched from 673 K to room temperature. As the stress amplitude increases further, oscillating dislocations overcome all Sr^{2+} ions (i.e., Sr^{2+} ions do not act as obstacles to the translational motion of dislocations) and the λ becomes constant. The $\Delta\tau$ value at which the ultrasonic oscillatory stress helps the dislocation break away from all weak obstacles is τ_{p2} . At a stress decrement more than τ_{p2} , forest dislocations remain as the obstacles to the mobile dislocation.

KCl crystal (nominal pure KCl crystal) may contain a small amount of various impurities (e.g., Cu max.2ppm, Pb max.2ppm, Fe max.2ppm, etc. in the reagent-grade powders), although none were added. As a result, the first bending point does not appear. The second bending point, however, appears because the amount of impurities is small.

3.3. Influence of the State of Sr^{2+} Ions on $\Delta\tau$ vs. λ Curve by Heat Treatment

Here is clarified the state of impurities in the specimen and is referred to the influence of the state of dopant ions on the interaction between a dislocation and the dopants, especially on the relation between temperature and the effective stress. The specimens used here are two kinds of single crystals. The first is KCl: Sr^{2+} (0.050 mol.% in the melt) in the preceding Section 2.1 and is hereafter named the quenched specimen. The second was prepared by keeping the quenched specimen at 370 K for 500 h and gradually cooling in a furnace for the purpose of aggregating dopants in it [85]. This is termed the annealed specimen here.

Dielectric absorption of an I-V dipole causes a peak on the $\tan\delta$ -frequency relation. The relative formula which gives the proportionality between the concentration of I-V dipoles and a Debye peak height is expressed by [86]

$$\tan \delta = \frac{2\pi e^2 c}{3\epsilon' a k T}, \text{ (maximum)} \quad (7)$$

where e is the elementary electric charge, c is the concentration of the I-V dipole, ϵ' is the dielectric constant in the matrix, and a is the lattice constant. Figure 13 shows the influence of this heat treatment on the $\tan\delta$ -frequency curves for KCl: Sr^{2+} at 393 K. The upper solid and dotted curves correspond to the quenched specimen and the lower curves the annealed specimen. Dotted lines show Debye peaks obtained by subtracting the d.c. part which is obtained by extrapolating the linear part of the

solid curves in the low-frequency region to the high-frequency region. Introducing the peak heights of the dotted curves into Equation (7), the concentration of the isolated dipole was determined to be 98.3 ppm for the quenched specimen and 21.8 ppm for the annealed specimen by dielectric loss measurement using an Andoh electricity TR-10C model. On the other hand, the atomic absorption gave 121.7 ppm for the Sr^{2+} concentration in the quenched specimen and 96.2 ppm for the annealed specimen. Therefore, it should be considered that 71.9% of the I-V dipoles turn into the aggregates in KCl: Sr^{2+} single crystal and form at least trimers [85] by the heat treatment. The trimer has a structure in which three dipoles (Sr^{2+} -vacancy- Sr^{2+} -vacancy- Sr^{2+} -vacancy) are arranged hexagonally head to tail in a (111) plane, as suggested by Cook and Dryden [85].

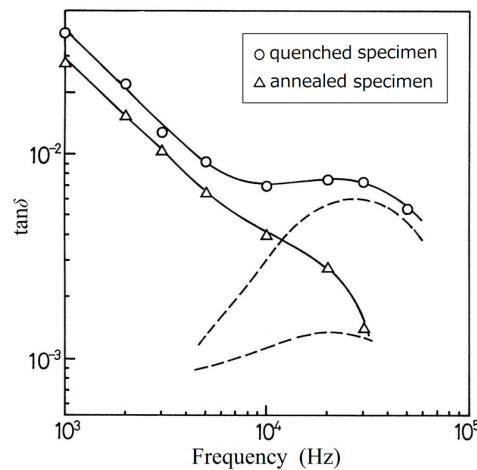


Figure 13. Dielectric loss in KCl containing Sr^{2+} ions at 393 K: (○) for the quenched specimen, (△) for the annealed specimen (reproduced from reference [87] with permission from the publisher). (---) Losses coming from the dipoles.

The $\Delta\tau$ vs. λ curves for the quenched specimen are already shown in Figures 8 and 10. The same phenomena as these figures are observed for the annealed specimens. That is to say, the curve has two bending points and two plateau regions and λ decreases with the $\Delta\tau$ between the two bending points at a given shear strain and temperature. The dependence of τ_{p1} and τ_{p2} on temperature for the quenched specimen is shown in Figure 14a, while that for the annealed specimen is shown in Figure 14b (the curves for τ_{p1} and τ_{p2} are to guide the reader's eye). The value of τ_{p1} becomes small by forming into the aggregates in the crystal and this result is clearer at lower temperature. This may be caused by the result that the separation between the weak obstacles lying on the mobile dislocation becomes wider as the I-V dipoles turn into aggregates. In addition, it is supposed that the decrease in τ_{p1} due to agglomerate of the I-V dipoles, i.e., softening, would be attributable to the loss of tetragonality (lattice distortion around the dopants) in terms of the Fleischer's model [74], as suggested by Chin et al. [1]. The decrease in the effective stress due to agglomerates of I-V dipoles has been reported for alkali halide crystals doped with divalent cations so far [1,13,75,88,89]. As for τ_{p2} , no great difference is seen between the quenched specimen and the annealed one. Accordingly, as the I-V dipoles turn into the aggregates by the heat treatment, the difference between τ_{p1} and τ_{p2} obviously becomes wider at lower temperature. This suggests that the distribution of Sr^{2+} obstacles on mobile dislocation, i.e., the average length of dislocation segments, for the annealed specimen is wider than that for the quenched one.

The critical temperature T_c at which τ_{p1} becomes zero and the dislocation breaks away from the dopants only with the help of thermal activation is around 210 K for the annealed specimen. This T_c value is small in contrast to $T_c \approx 240$ K for the quenched specimen as can be seen from Figure 14a,b.

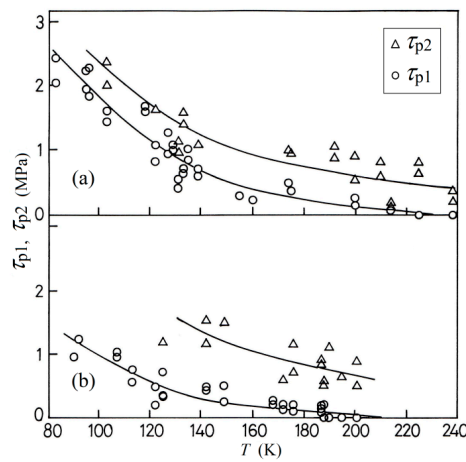


Figure 14. Dependence of (○) τ_{p1} and (△) τ_{p2} on temperature for KCl:Sr²⁺ (reproduced from reference [87] with permission from the publisher): (a) for the quenched specimen; (b) for the annealed specimen.

3.4. Activation Energy for the Break-Away of a Dislocation from the Dopant Ion

The thermally activated deformation rate is expressed by an Arrhenius-type equation:

$$\dot{\epsilon} = \dot{\epsilon}_0 \exp\left(\frac{-G}{kT}\right) \quad (8)$$

where $\dot{\epsilon}_0$ is a frequency factor and is unique for a particular dislocation mechanism. G is the activation energy for overcoming of local barrier (i.e., the dopant in here) by a dislocation at temperature T . It is assumed that the interaction between a dislocation and the dopant ion (i.e., I-V dipole) for the quenched specimen can be approximated to the Fleischer's model [74] taking account of the Friedel relation [80]. The model is named F - F here. Then, the relative formula of τ_{p1} and temperature, which will reveal the force–distance relation between a dislocation and a weak obstacle, is given by

$$\left(\frac{\tau_{p1}}{\tau_{p0}}\right)^{1/3} = 1 - \left(\frac{T}{T_c}\right)^{1/2} \quad (9)$$

where τ_{p0} is the value of τ_{p1} at absolute zero.

The activation energy for the interaction between a dislocation and the obstacle is expressed from the Arrhenius-type equation for the thermally activated deformation rate at low temperature as the Equation (8), namely

$$G = \alpha kT, \quad \left(\alpha = \ln\left(\frac{\dot{\epsilon}_0}{\dot{\epsilon}}\right)\right) \quad (10)$$

and the G for the F - F is also expressed by [90]

$$G = G_0 \left\{ 1 - \left(\frac{\tau^*}{\tau_0^*}\right)^{1/3} \right\}^2, \quad (G_0 = F_0 b) \quad (11)$$

where G_0 is the Gibbs free energy for the break-away of a dislocation from the dopant in the absence of an applied stress, τ_0^* is the effective shear stress (τ^*) at absolute zero, and F_0 is the force acted on the dislocation at 0 K. Differentiating the combination of Equations (10) and (11) with respect to the shear stress gives

$$\frac{\partial \ln \dot{\epsilon}}{\partial \tau^*} = \left(\frac{2G_0}{3kT\tau_0^*}\right) \left(\frac{\tau_0^*}{\tau^*}\right)^{2/3} \left\{ 1 - \left(\frac{\tau^*}{\tau_0^*}\right)^{1/3} \right\} + \frac{\partial \ln \dot{\epsilon}_0}{\partial \tau^*} \quad (12)$$

Further, substituting Equation (9) in Equation (12) gives

$$\frac{\partial \ln \dot{\epsilon}}{\partial \tau^*} = \left(\frac{2G_0}{3kT\tau_{p0}} \right) \left\{ 1 - \left(\frac{T}{T_c} \right)^{1/2} \right\}^{-2} \left(\frac{T}{T_c} \right)^{1/2} + \frac{\partial \ln \dot{\epsilon}_0}{\partial \tau^*} \quad (13)$$

where τ_0^* is replaced by τ_{p0} . The result of calculations of Equation (13) for the F-F is shown in Figure 15 for the quenched specimen and the solid line is determined using the least squares method so as to fit to the experimental data (open symbols). The open symbols correspond to the λ_p^{-1} for the quenched specimen. On the basis of the slope of straight line, the G_0 is 0.39 eV. The strain-rate sensitivity due to weak obstacles, λ_p , is defined in Figure 8. It is assumed from the following two more experimental results in addition to the description in the Section 1 (introduction) that λ_p is the strain-rate sensitivity due to Sr^{2+} obstacles. Firstly, the $\Delta\tau$ vs. λ curve shifts upward with increasing shear strain, while λ_p is almost constant independently of the strain as shown in Figure 8 for $\text{KCl}:\text{Sr}^{2+}$ (0.050 mol.%) at several strains and 200 K. Secondly, λ_p is proportional to the square root of Sr^{2+} concentration ($c^{1/2}$), which is related to the inverse of the average length L of the dislocation segments (i.e., $\lambda_p = kT/bLd$), at a given temperature. This is shown in Figure 16. The concentration of the I-V dipole was estimated by the dielectric loss measurement.

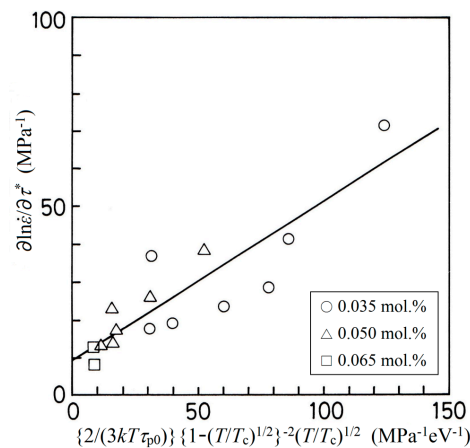


Figure 15. Linear plots of Equation (13) for the quenched specimen: $\text{KCl}:\text{Sr}^{2+}$ (\circ) 0.035 mol.%, (\triangle) 0.050 mol.%, (\square) 0.065 mol.% in the melt (reproduced from reference [90] with permission from the publisher).

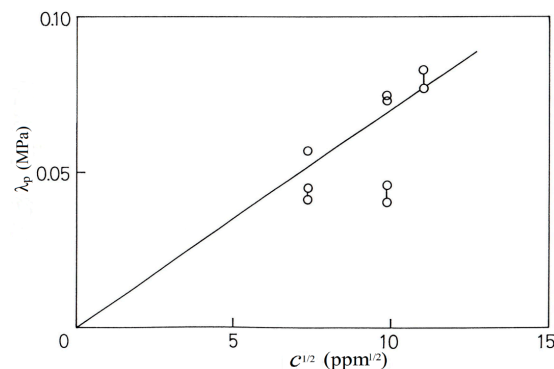


Figure 16. Relationship between λ_p and $c^{1/2}$ for $\text{KCl}:\text{Sr}^{2+}$ at the temperatures of 120 to 130 K (reproduced from reference [83] with permission from the publisher).

As for the annealed specimen, the G_0 is obtained as follows. The G is expressed for square force–distance relation between a dislocation and a weak obstacle as follows

$$G = G_0 - \tau^* Lbd \quad (14)$$

From the Fridel relation [80], the average spacing of weak obstacles along the dislocation is

$$L = \left(\frac{2L_0^2 E}{\tau^* b} \right)^{1/3} \quad (15)$$

where L_0 is the average spacing of weak obstacles on the slip plane and E is the line tension of the dislocations. Substituting Equation (15) into Equation (14), the Gibbs free energy is given by

$$G = G_0 - \beta \tau^{*2/3}, \quad \left(\beta = \left(2\mu b^4 d^3 L_0^2 \right)^{1/3} \right) \quad (16)$$

Differentiating the substitutional equation of Equation (16) in Equation (8) with respect to the shear stress, we find

$$\tau_{p1} \left(\frac{\partial \ln \dot{\epsilon}}{\partial \tau^*} \right) = \left(\frac{2G_0}{3kT} \right) + \frac{2}{3} \ln \left(\frac{\dot{\epsilon}}{\dot{\epsilon}_0} \right) \quad (17)$$

where τ^* is replaced by τ_{p1} . The result of calculations of Equation (17) is shown in Figure 17 for the annealed specimen, where the solid line is given using the least squares method and the open circles are obtained from τ_{p1}/λ_p . The interaction energy G_0 between a dislocation and the aggregate of I-V dipoles in the specimen, which is obtained from the slope of straight line in Figure 17, is 0.26 eV. The Gibbs free energy for the annealed specimen is smaller than that for the quenched one as tabulated in Table 1.

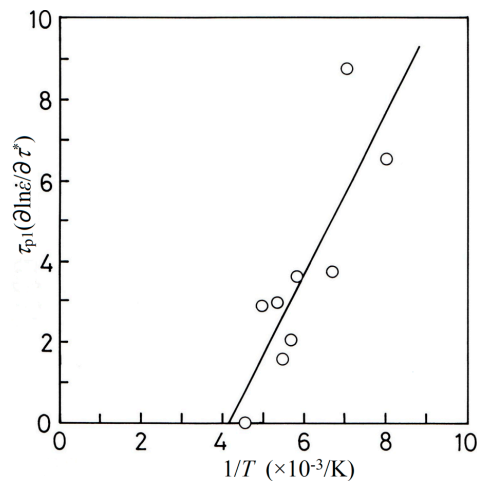


Figure 17. Linear plots of Equation (17) for the annealed specimen (reproduced from reference [91] with permission from the publisher).

Table 1. Values of G_0 for the quenched and the annealed specimens.

| Specimen | G_0 (eV) |
|-------------------|------------|
| Quenched specimen | 0.39 |
| Annealed specimen | 0.26 |

3.5. Strain-Rate Sensitivity at the Second Plateau Place on the $\Delta\tau$ vs. λ Curve

Three-stage strain hardening has been clearly established as the characteristic behavior of single crystals of rock salt structure, deforming predominantly by single glide [92]. The three-stage strain hardening is obtained for KCl [93,94]. It is also observed for the quenched and the annealed specimens. Each of the three-stages for the specimens is illustrated in Figure 18, which is generally denoted by stage I, II, and III as shown in the figure. The variation of strain-rate sensitivity at the second plateau place on the $\Delta\tau$ vs. λ curve with shear strain (see the marked part with grey circle in Figure 19 illustrated the relative curve between $\Delta\tau$ and λ), where the obstacles to a dislocation motion are only forest dislocations and the dopant ions no longer act as obstacles, is investigated in the different plastic deformation regions of stress-strain curve for the two kinds of specimens, namely, the quenched specimen and the annealed one. The size of specimens used here is within $(5 \pm 1) \times (5 \pm 1) \times (15 \pm 1) \text{ mm}^3$. Because, it has been reported that the height–width of specimens determines the shape of the work-hardening curve in the compression at a constant strain rate and temperature for CaF_2 single crystals [95] and besides glide geometry is directly related to the shape and size of KCl crystals [2]. The variation of λ at the second plateau place on the $\Delta\tau$ vs. λ curve with shear strain is shown in Figure 20. The $\Delta\lambda/\Delta\varepsilon$ seems to be the variation of the strain-rate sensitivity due to dislocation cuttings with shear strain. The relations of temperature and $\Delta\lambda/\Delta\varepsilon$ in stage I and in stage II of stress-strain curve are represented by a circle and a triangle, respectively. The open symbols correspond to that for the quenched specimen and the solid ones that for the annealed specimen. The full lines in this figure are to guide the reader's eye. Unfortunately, the $\Delta\lambda/\Delta\varepsilon$ could not be obtained at low temperature. The $\Delta\lambda/\Delta\varepsilon$ in stage II is obviously larger than that in stage I at a given temperature. And the values of $\Delta\lambda/\Delta\varepsilon$ in stage I and in stage II increase with decreasing temperature. Figure 20 also shows that the $\Delta\lambda/\Delta\varepsilon$ for the annealed specimens is considerably large in contrast to that for the quenched specimens in the two stages at the temperature. This may result from a rapid increase in forest dislocation density with shear strain in the annealed specimen. Accordingly, the increase in it in the annealed specimen seems to be remarkable in the two stages under the compression test, compared with it in the quenched specimen. According to Michalak [96] some dislocation cutting process becomes an important hardening mechanism and the strain-hardening increases. If the consideration about forest dislocation density for the two kinds of specimens is accurate, it is expected that a strain-hardening rate ($d\tau/d\varepsilon$) for the annealed specimen is larger than that for the quenched specimen at a given temperature and shear strain.

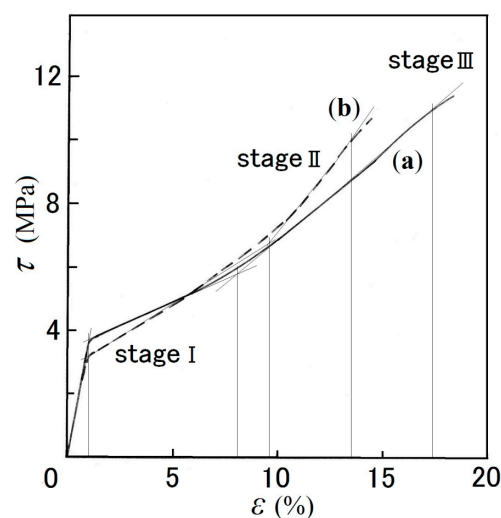


Figure 18. Shear stress-shear strain curves for (a) (—) the quenched specimen at 175 K and (b) (- - -) the annealed specimen at 176 K.

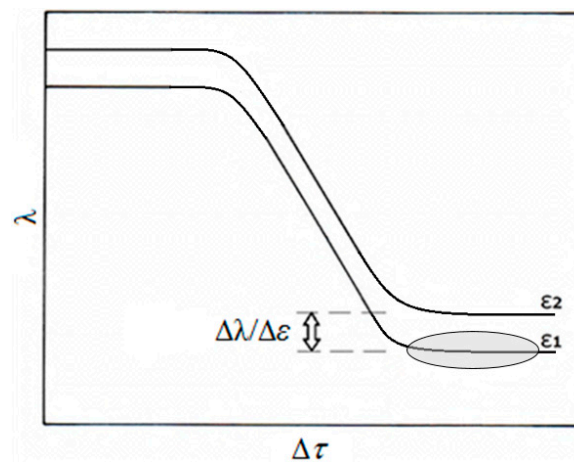


Figure 19. Illustration of relationship between the strain-rate sensitivity of flow stress and the stress decrement due to the superimposition of ultrasonic oscillation at a given strain, ϵ ($\epsilon_1 < \epsilon_2$). $\Delta\lambda/\Delta\epsilon$ represents the variation of the strain-rate sensitivity due to dislocation cuttings with shear strain.

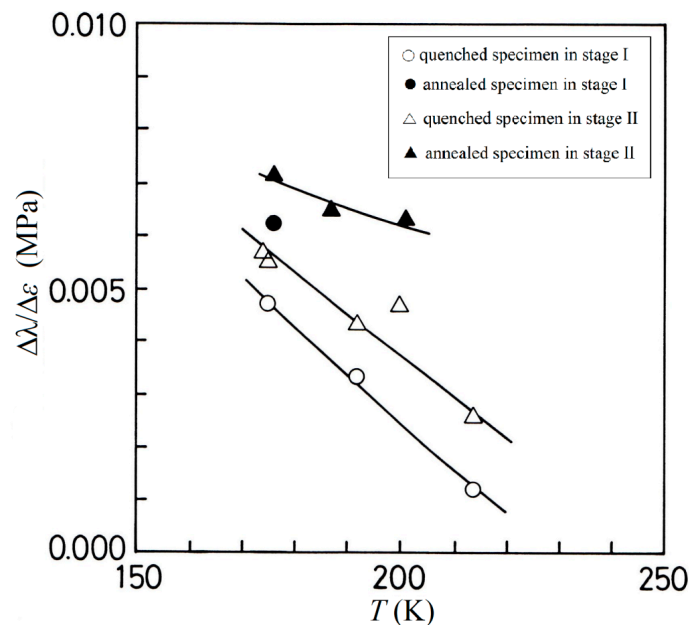


Figure 20. Dependence of $\Delta\lambda/\Delta\epsilon$ on the temperature in the different plastic deformation regions: (○) for the quenched specimen and (●) for the annealed specimen in stage I; (△) for the quenched specimen and (▲) for the annealed specimen in stage II (reproduced from reference [97] with permission from the publisher).

When the whole crystal is filled with primary dislocation dipoles and multipoles, stage I of stress-strain curve ends and the stage II, which is characterized by the onset of glide on oblique systems, follows. Afterwards, the stage III, which is probably associated with the cross glide of screw dislocation around obstacles, ensues in the process of plastic deformation [92]. Accordingly, it will be also expected that the extent of stage I and stage II for the annealed specimen is shorter than that for the quenched specimen at a given temperature.

The relation between $d\tau/d\epsilon$ and temperature for the two kinds of specimens is shown in Figure 21a for stage I and b for stage II of the plastic deformation regions. The value of $d\tau/d\epsilon$ in stage II is about two times larger than that in stage I at a given temperature for both the specimens. Furthermore, the $d\tau/d\epsilon$ for the annealed specimen is obviously large as against that for the quenched specimen in the

two stages as can be seen from Figure 21a,b. Although the extent of stage I is further investigated for the two kinds of specimens, the difference between the extents of it could not be found out within the temperature. While the extent of stage II could not also be made a comparison between them, because most of the specimens were fractured within stage II by the compression test at low temperature. Then, we attempted to investigate the extent between shear strains of yield point and of fractured point, i.e., plastic deformation region, at various temperatures. The result of the extent of plastic deformation region is shown in Figure 22. The open circles and the solid ones correspond to those for the quenched specimen and for the annealed specimen, respectively. The extent of it tends to be large with increasing temperature for both the specimens. Figure 22 also shows that the extent of it for the annealed specimen seems to be shorter than it for the quenched specimen at a given temperature. Consequently, it is clear that the increase in forest dislocation density in the annealed specimen is remarkable in contrast to it in the quenched specimen under the compression test. This may be attributed to the phenomenon that a small amount of the much larger aggregates than trimers, which are contained in the annealed specimen, contribute to the increase in forest dislocation density.

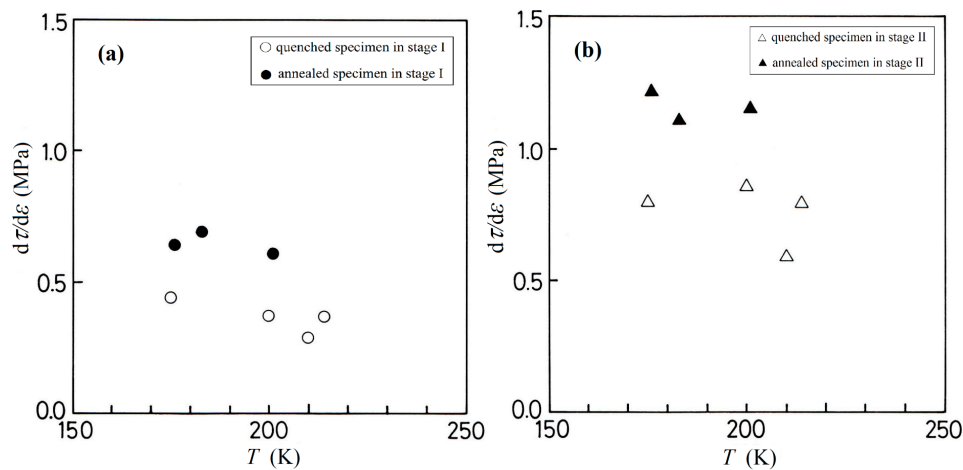


Figure 21. Dependence of the strain-hardening rate on the temperature in the different plastic deformation regions (reproduced from reference [97] with permission from the publisher): (a) (○) for the quenched specimen and (●) for the annealed specimen in stage I; (b) (△) for the quenched specimen and (▲) for the annealed specimen in stage II.

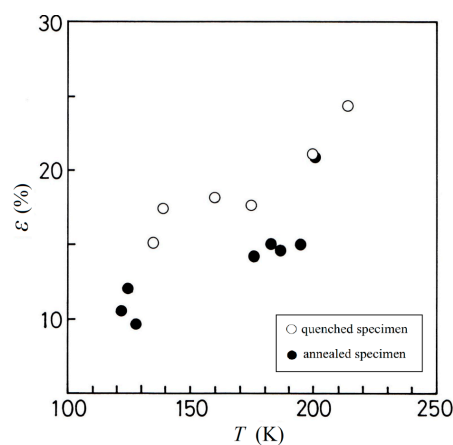


Figure 22. Dependence of the extent of plastic deformation region on the temperature for both the specimens: (○) for the quenched specimen and (●) for the annealed specimen (reproduced from reference [97] with permission from the publisher).

4. Summary

By the original method which combines strain-rate cycling tests with the Blaha effect measurement, the dislocation-Sr²⁺ ions (I-V dipoles) interaction has been investigated during the plastic deformation of bulk material (KCl:Sr²⁺ single crystal). The data obtained by the original method is sensitive to a change in the state of dopant ions in the specimen by heat treatment, as reviewed in the each Sections 3.3–3.5. The following results are reviewed mainly on the basis of $\Delta\tau$ vs. λ curves derived from the original method.

In Sections 3.1 and 3.2, we reviewed the process of the measurement of strain-rate sensitivity under the application of ultrasonic oscillatory stress in detail. The plots of the strain-rate sensitivity and the stress decrement due to oscillation has two bending points and two plateau regions for KCl:Sr²⁺ and seem to reflect the influence of ultrasonic oscillation on the dislocation motion on the slip plane. The first bending point, τ_{p1} , at low stress decrement corresponds to the effective stress due to Sr²⁺ ions on the mobile dislocation.

In Section 3.3, we reviewed the influence of the state of dopant ions on the effective stress due to the Sr²⁺ ions in KCl:Sr²⁺ single crystals. If the dopant ions in KCl:Sr²⁺ single crystals diffuse into the matrix, or they aggregate by the heat treatment, various deformation characteristics (τ_{p1} and T_c) become changed. This is because the state of a small amount of dopants in the crystals strongly influences the resistance to movement of a dislocation.

In Section 3.4, the change in obstacle size due to the agglomeration of I-V dipoles was reviewed as an influential factor of the Gibbs free energy for overcoming the local barrier by a dislocation after the heat treatment. The specimens used here are two kinds of heat-treated ones, i.e., the quenched and the annealed KCl:Sr²⁺ (0.050 mol.% in the melt) single crystals. The G_0 value (0.26 eV) for the annealed specimen is smaller than that (0.39 eV) for the quenched one.

In Section 3.5, we reviewed the remarkable increase in density of the forest dislocation under the compression test by annealing the quenched specimen. This is examined from the variation of strain-rate sensitivity at the second plateau place on the $\Delta\tau$ vs. λ curve with shear strain in both stage I and stage II of stress-strain curve at the temperatures of 170 to 220 K. As a proof, the experimental results on the strain-hardening rate and on the extent of plastic deformation region are obtained for the two kinds of the specimens (i.e., the quenched specimen and the annealed one).

The strain-rate cycling test during the Blaha effect measurement has been successively provided the information on the dislocation motion breaking away from the strain fields around dopant ions with the help of thermal activation, and seems to separate the contributions arising from the interaction between dislocation and the point defects and those from dislocations themselves during plastic deformation of ionic crystals. Such information on dislocation motion in bulk material cannot be obtained by the widely known methods, e.g., the measurements of yield stress and proof stress, micro-hardness tests, direct observations of dislocation, internal friction measurements, or stress relaxation tests. However, the original method (the strain-rate cycling test during the Blaha effect measurement) is different from above-mentioned ones and would be possible to clear it up.

Conflicts of Interest: The author declares no conflict of interest.

References

1. Chin, G.Y.; Van Uitert, L.G.; Green, M.L.; Zydzik, G.J.; Kometani, T.Y. Strengthening of Alkali Halides by Divalent-ion Additions. *J. Am. Ceram. Soc.* **1973**, *56*, 369–372. [[CrossRef](#)]
2. Suszyńska, M. Effect of Impurity Concentration and Plastic Deformation on Dislocation Density of KCl Crystals. *Kristall. Technik.* **1974**, *9*, 1199–1207. [[CrossRef](#)]
3. Kataoka, T.; Yamada, T. Yield Strength and Dislocation Mobility of KCl-KBr Solid Solution Single Crystals. *Jpn. J. Appl. Phys.* **1977**, *16*, 1119–1126. [[CrossRef](#)]
4. Boyarskaya, Y.S.; Zhitaru, R.P.; Palistrant, N.A. The anomalous behaviour of the doped NaCl crystals compressed at low temperatures. *Cryst. Res. Technol.* **1990**, *25*, 1469–1473. [[CrossRef](#)]

5. Boyarskaya, Y.S.; Zhitaru, R.P.; Palistrant, N.A. Influence of the state of the impurity on the deformation-rate dependence of the yield stress of NaCl:Ca single crystals. *Sov. Phys. Solid State* **1990**, *32*, 1989–1990.
6. Okazaki, K. Solid-solution hardening and softening in binary iron alloys. *J. Mater. Sci.* **1996**, *31*, 1087–1099. [[CrossRef](#)]
7. Tabachnikova, E.D.; Podolskiy, A.V.; Smirnov, S.N.; Psaruk, I.A.; Liao, P.K. Temperature dependent mechanical properties and thermal activation plasticity of nanocrystalline and coarse grained Ni-18.75 at.% Fe alloy. *IOP Conf. Ser. Mater. Sci. Eng.* **2014**, *63*, 012105. [[CrossRef](#)]
8. Pratt, P.L.; Harrison, R.P.; Newey, C.W.A. Dislocation mobility in ionic crystals. *Disc. Faraday Soc.* **1964**, *38*, 211–217. [[CrossRef](#)]
9. Newey, C.W.A.; Harrison, R.P.; Pratt, P.L. Precipitation Hardening and Dislocation Locking in Doped NaCl. *Proc. Brit. Ceram. Soc.* **1966**, *6*, 305–316.
10. Chin, G.Y.; Van Uitert, L.G.; Green, M.L.; Zydzik, G. Hardness, Yield Strength and Young's Modulus in Halide Crystals. *Scripta Metall.* **1972**, *6*, 475–480. [[CrossRef](#)]
11. Green, M.L.; Zydzik, G. Effect of heat treatment on the microhardness of some mixed and doped alkali halides. *Scripta Metall.* **1972**, *6*, 991–994. [[CrossRef](#)]
12. Andreev, G.A.; Klimov, V.A. Influence of the State of an Impurity on the Microhardness of NaCl:Sr Single Crystals. *Sov. Phys. Solid State* **1980**, *22*, 2042–2043.
13. Buravleva, M.G.; Rozenberg, G.K.; Soifer, L.M.; Chaikovskii, E.F. Changes in the flow stress of LiF:Mg²⁺ and LiF:Co²⁺ crystals during precipitation of solid solutions. *Sov. Phys. Solid State* **1980**, *22*, 150–152.
14. Narasimha Reddy, K.; Subba Rao, U.V. Influence of Gadolinium Impurity on Microhardness of Host Alkali Halide Crystal. *Cryst. Res. Technol.* **1984**, *19*, K73–K76. [[CrossRef](#)]
15. Strunk, H. Investigation of Cross-slip Events in NaCl Crystals by Transmission Electron Microscopy. *Phys. Status Solidi (a)* **1975**, *28*, 119–126. [[CrossRef](#)]
16. Appel, F.; Messerschmidt, U. The interaction between dislocations and point obstacles: A comparison of the interaction parameter distributions obtained from computer simulation and from in situ high voltage electron microscopy straining experiments. *Mater. Sci. Eng.* **1982**, *52*, 69–74. [[CrossRef](#)]
17. Messerschmidt, U.; Appel, F.; Schmid, H. The radius of curvature of dislocation segments in MgO crystals stressed in the high-voltage electron microscope. *Philos. Mag. A* **1985**, *51*, 781–796. [[CrossRef](#)]
18. Kataoka, T.; Ohji, H.; Morishita, H.; Kishida, K.; Azuma, K.; Yamada, T. In-situ observation of moving dislocations in KCl crystal by laser-light topography. *Jpn. J. Appl. Phys.* **1989**, *28*, L697–L700. [[CrossRef](#)]
19. Kataoka, T.; Ohji, H.; Kishida, K.; Azuma, K.; Yamada, T. Direct observation of glide dislocations in a KCl crystal by the light scattering method. *Appl. Phys. Lett.* **1990**, *56*, 1317–1319. [[CrossRef](#)]
20. Kataoka, T. The light scattering topography method: Direct observation of moving dislocations. *Butsuri* **1992**, *47*, 713–716. (In Japanese)
21. Messerschmidt, U. *Dislocation Dynamics during Plastic Deformation*; Springer: Berlin, Heidelberg, 2010.
22. Indenbom, V.L.; Chernov, V.M. Determination of characteristics for the interaction between point defects and dislocations from internal friction experiments. *Phys. Status Solidi (a)* **1972**, *14*, 347–354. [[CrossRef](#)]
23. Schwarz, R.B.; Granato, A.V. Measurement of the force-distance profile for the interaction between a dislocation and a point defect. *Phys. Rev. Lett.* **1975**, *34*, 1174–1177. [[CrossRef](#)]
24. Ivanov, V.I.; Lebedev, A.B.; Kardashev, B.K.; Nikanorov, S.P. Interaction of dislocations with pinning centers in magnesium at temperatures 295–4.2K. *Sov. Phys. Solid State* **1986**, *28*, 867–868.
25. Kosugi, T.; Kino, T. Experimental Determination of the Force-Distance Relation for the Interaction between a Dislocation and a Solute Atom. *J. Phys. Soc. Jpn.* **1987**, *56*, 999–1009. [[CrossRef](#)]
26. Kosugi, T. Temperature Dependence of Amplitude-dependent Internal Friction due to Simultaneous Breakaway of a Dislocation from Several Pinning Points. *Mater. Sci. Eng. A* **2001**, *309–310*, 203–206. [[CrossRef](#)]
27. Gremaud, G. Dislocation-Point Defect Interactions. *Mater. Sci. Forum* **2001**, *366–368*, 178–246. [[CrossRef](#)]
28. Dotsenko, V.I. Stress Relaxation in Crystals. *Phys. Status Solidi (b)* **1979**, *93*, 11–43. [[CrossRef](#)]
29. Urusovskaya, A.A.; Petchenko, A.M.; Mozgovoi, V.I. The influence of strain rate on stress relaxation. *Phys. Status Solidi (a)* **1991**, *125*, 155–160. [[CrossRef](#)]
30. Johnston, W.G.; Gilman, J.J. Dislocation velocities, dislocation densities, and plastic flow in lithium fluoride crystals. *J. Appl. Phys.* **1959**, *30*, 129–144. [[CrossRef](#)]

31. Granato, A.V.; Lücke, K. Theory of mechanical damping due to dislocations. *J. Appl. Phys.* **1956**, *27*, 583–593. [[CrossRef](#)]
32. Blaha, F.; Langenecker, B. Dehnung von Zink-Kristallen unter Ultraschalleinwirkung. *Naturwiss.* **1955**, *42*, 556. [[CrossRef](#)]
33. Nevill, G.E.; Brotzen, F.R. The effect of vibrations on the static yield strength of low-carbon steel. *Proc. ASTM* **1957**, *57*, 751–758.
34. Langenecker, B. Effects of ultrasound on deformation characteristics of metals. *IEEE Trans. Sonic Ultrasonic* **1966**, *13*, 1–8. [[CrossRef](#)]
35. Izumi, O.; Oyama, K.; Suzuki, Y. Effects of superimposed ultrasonic vibration on compressive deformation of metals. *Trans. JIM* **1966**, *7*, 162–167. [[CrossRef](#)]
36. Evans, A.E.; Smith, A.W.; Waterhouse, W.J.; Sansome, D.H. Review of the application of ultrasonic vibrations to deforming metals. *Ultrasonics* **1975**, *13*, 162–170.
37. Jimma, T.; Kasuga, Y.; Iwaki, N.; Miyazawa, O.; Mori, E.; Ito, K.; Hatano, H. An application of ultrasonic vibration to the deep drawing process. *J. Mater. Process. Technol.* **1998**, *80–81*, 406–412. [[CrossRef](#)]
38. Susan, M.; Bujoreanu, L.G. The metal-tool contact friction at the ultrasonic vibration drawing of ball-bearing steel wires. *Rev. Metal. Madrid* **1999**, *35*, 379–383. [[CrossRef](#)]
39. Murakawa, M.; Jin, M. The utility of radially and ultrasonically vibrated dies in the wire drawing process. *J. Mater. Process. Technol.* **2001**, *113*, 81–86. [[CrossRef](#)]
40. Susan, M.; Bujoreanu, L.G.; Gălușcă, D.G.; Munteanu, C.; Mantu, M. On the drawing in ultrasonic field of metallic wires with high mechanical resistance. *J. Optoelectron. Adv. Mater.* **2005**, *7*, 637–645.
41. Lucas, M.; Gachagan, A.; Cardoni, A. Research applications and opportunities in power ultrasonics. *Proc. IMechE Part C J. Mech. Eng. Sci.* **2009**, *223*, 2949–2965. [[CrossRef](#)]
42. Siddiq, A.; El Sayed, T. Ultrasonic-assisted manufacturing processes: Variational model and numerical simulations. *Ultrasonics* **2012**, *52*, 521–529. [[CrossRef](#)] [[PubMed](#)]
43. Makhdum, F.; Phadnis, V.A.; Roy, A.; Silberschmidt, V.V. Effect of ultrasonically-assisted drilling on carbon-fibre-reinforced plastics. *J. Sound Vib.* **2014**, *333*, 5939–5952. [[CrossRef](#)]
44. Graff, K.F. Ultrasonic Metal Forming: Processing. In *Power Ultrasonics: Applications of High-intensity Ultrasound*; Gallego-Juarez, J.A., Graff, K.F., Eds.; Elsevier: Cambridge, UK, 2015; pp. 377–438.
45. Puškár, A. Effect of grain size, cold work, loading frequency and temperature on fatigue limit of mild steel. *Metallurg. Trans.* **1976**, *7A*, 1529–1533. [[CrossRef](#)]
46. Jon, M.C.; Mason, W.P.; Beshers, D.N. Internal friction during ultrasonic deformation of alpha-brass. *J. Appl. Phys.* **1976**, *47*, 2337–2349. [[CrossRef](#)]
47. Shetty, D.K.; Meshii, M. Plastic deformation of aluminum under repeated loading. *Metallurg. Trans.* **1975**, *6A*, 349–366. [[CrossRef](#)]
48. Bradley, W.L.; Nam, S.W.; Matlock, D.K. Fatigue perturbed creep of pure aluminum at ambient temperatures. *Metallurg. Trans.* **1976**, *7A*, 425–430. [[CrossRef](#)]
49. Lebedev, A.B.; Kustov, S.B.; Kardashev, B.K. Amplitude-dependent ultrasound absorption and acoustoplastic effect during active deformation of sodium chloride crystals. *Sov. Phys. Solid State* **1982**, *24*, 1798–1799.
50. Baker, G.S.; Carpenter, S.H. Dislocation mobility and motion under combined stresses. *J. Appl. Phys.* **1967**, *38*, 1586–1591. [[CrossRef](#)]
51. Kaiser, G.; Pechhold, W. Dynamic-mechanical investigations for the study of dislocation motion during plastic flow. *Acta Metall.* **1967**, *17*, 527–537. [[CrossRef](#)]
52. Suzuki, T. Effects of vibrational stress on static flow stress (I). *Seisan-Kenkyu* **1970**, *22*, 194–197. (In Japanese)
53. Suzuki, T. Effects of vibrational stress on static flow stress (II). *Seisan-Kenkyu* **1970**, *22*, 344–347. (In Japanese)
54. Endo, T.; Suzuki, K.; Ishikawa, M. Effects of superimposed ultrasonic oscillatory stress on the deformation of Fe and Fe-3%Si alloy. *Trans. Japan Inst. Metals* **1979**, *20*, 706–712. [[CrossRef](#)]
55. Endo, T.; Tasaki, M.; Kubo, M.; Shimada, T. High temperature deformation of an Al-5at%Mg alloy under combined high frequency stresses. *J. Japan Inst. Met. Mater.* **1982**, *46*, 773–779. (In Japanese) [[CrossRef](#)]
56. Lebedev, A.B.; Kustov, S.B.; Kardashev, B.K. Investigation of the amplitude-dependent internal friction during plastic deformation of sodium chloride single crystals. *Sov. Phys. Solid State* **1983**, *25*, 511–512.
57. Ohgaku, T.; Takeuchi, N. The relation of the Blaha effect with internal friction for alkali halide crystals. *Phys. Status Solidi (a)* **1988**, *105*, 153–159. [[CrossRef](#)]

58. Hikata, A.; Johnson, R.A.; Elbaum, C. Interaction of dislocations with electrons and with phonons. *Phys. Rev.* **1970**, *B2*, 4856–4863. [[CrossRef](#)]
59. Ohgaku, T.; Takeuchi, N. The Blaha effect of alkali halide crystals. *Phys. Status Solidi (a)* **1987**, *102*, 293–299. [[CrossRef](#)]
60. Hesse, J.; Hobbs, L.W. Dislocation density in highly deformed NaCl single crystals. *Phys. Status Solidi (a)* **1972**, *14*, 599–604. [[CrossRef](#)]
61. Frank, W. Theorie der Verfestigung von Alkalihalogenid-Einkristallen I. Qualitative betrachtungen. *Mater. Sci. Eng.* **1970**, *6*, 121–131. [[CrossRef](#)]
62. Frank, W. Theorie der Verfestigung von Alkalihalogenid-Einkristallen II. Quantitative formulierung. *Mater. Sci. Eng.* **1970**, *6*, 132–148. [[CrossRef](#)]
63. Ohgaku, T.; Takeuchi, N. Relation between plastic deformation and the Blaha effect for alkali halide crystals. *Phys. Status Solidi (a)* **1989**, *111*, 165–172. [[CrossRef](#)]
64. Li, J.C.M. Kinetics and Dynamics in Dislocation Plasticity. In *Dislocation Dynamics*; Rosenfield, A.R., Hahn, G.T., Bemont, A.L., Jaffee, R.I., Eds.; Mc Graw-Hill Publ. Co.: New York, NY, USA, 1968; pp. 87–116.
65. Ohgaku, T.; Takeuchi, N. Interaction between a dislocation and monovalent impurities in KCl single crystals. *Phys. Status Solidi (a)* **1992**, *134*, 397–404. [[CrossRef](#)]
66. Ohgaku, T.; Teraji, H. Investigation of interaction between a dislocation and a Br⁻ ion in NaCl:Br⁻ single crystals. *Phys. Status Solidi (a)* **2001**, *187*, 407–413. [[CrossRef](#)]
67. Argon, A.S.; Nigam, A.K.; Padawer, G.E. Plastic deformation and strain hardening in pure NaCl at low temperatures. *Philos. Mag.* **1972**, *25*, 1095–1118. [[CrossRef](#)]
68. Young, F.W., Jr. Etch pits at dislocations in copper. *J. Appl. Phys.* **1961**, *32*, 192–201. [[CrossRef](#)]
69. Takeuchi, S. Solid-Solution strengthening in single crystals of iron alloys. *J. Phys. Soc. Jap.* **1969**, *27*, 929–940. [[CrossRef](#)]
70. Sprackling, M.T. *The Plastic Deformation of Simple Ionic Crystals*; Alper, A.M., Margrave, J.L., Nowick, A.S., Eds.; Academic Press: London, UK, 1976.
71. Zakrevskii, V.A.; Shul'diner, A.V. Dislocation interaction with radiation defects in alkali-halide crystals. *Phys. Sol. Stat.* **2000**, *42*, 270–273. [[CrossRef](#)]
72. Katoh, S. Influence of impurity concentration on the Blaha effect. Bachelor's Thesis, Kanazawa University, Kanazawa, Japan, 1987; pp. 16–21.
73. Pick, H.; Weber, H. Dichteänderung von KCl-Kristallen durch Einbau zweiwertiger Ionen. *Z. Phys.* **1950**, *128*, 409–413. [[CrossRef](#)]
74. Fleischer, R.L. Rapid solution hardening, dislocation mobility, and the flow stress of crystals. *J. Appl. Phys.* **1962**, *33*, 3504–3508. [[CrossRef](#)]
75. Dryden, J.S.; Morimoto, S.; Cook, J.S. The hardness of alkali halide crystals containing divalent ion impurities. *Philos. Mag.* **1965**, *12*, 379–391. [[CrossRef](#)]
76. Orozco, M.E.; Mendoza, A.A.; Soullard, J.; Rubio, O.J. Changes in yield stress of NaCl:Pb²⁺ crystals during dissolution and precipitation of solid solutions. *Jpn. J. Appl. Phys.* **1982**, *21*, 249–254. [[CrossRef](#)]
77. Zaldo, C.; Solé, J.G.; Agulló-López, F. Mechanical strengthening and impurity precipitation behaviour for divalent cation-doped alkali halides. *J. Mater. Sci.* **1982**, *17*, 1465–1473. [[CrossRef](#)]
78. Reddy, B.K. Annealing and ageing studies in quenched KBr:Ba²⁺ single crystals. *Phys. Status Solidi (a)* **1987**, *99*, K7–K10. [[CrossRef](#)]
79. Sirdeshmukh, D.B.; Sirdeshmukh, L.; Subhadra, K.G. *Alkali Halides*; Hull, R., Osgood, R.M., Jr., Sakaki, H., Zunger, A., Eds.; Springer-Verlag: Berlin, Germany, 2001; p. 41.
80. Friedel, J. *Dislocations*; Pergamon Press: Oxford, UK, 1964; p. 224.
81. Stoloff, N.S.; Lezius, D.K.; Johnston, T.L. Effect of temperature on the deformation of KCl-KBr alloys. *J. Appl. Phys.* **1963**, *34*, 3315–3322. [[CrossRef](#)]
82. Kohzuki, Y.; Ohgaku, T.; Takeuchi, N. Interaction between a dislocation and impurities in KCl single crystals. *J. Mater. Sci.* **1993**, *28*, 3612–3616. [[CrossRef](#)]
83. Kohzuki, Y.; Ohgaku, T.; Takeuchi, N. Interaction between a dislocation and various divalent impurities in KCl single crystals. *J. Mater. Sci.* **1995**, *30*, 101–104. [[CrossRef](#)]
84. Ohgaku, T.; Takeuchi, N. Study on dislocation-impurity interaction by the Blaha effect. *Phys. Status Solidi (a)* **1990**, *118*, 153–159. [[CrossRef](#)]

85. Cook, J.S.; Dryden, J.S. An investigation of the aggregation of divalent cationic impurities in alkali halides by dielectric absorption. *Proc. Phys. Soc.* **1962**, *80*, 479–488. [[CrossRef](#)]
86. Lidiard, A.B. Ionic Conductivity. In *Handbuch der Physik*; Springer: Berlin, Germany, 1957; Volume 20, pp. 246–349.
87. Kohzuki, Y.; Ohgaku, T.; Takeuchi, N. Influence of a state of impurities on the interaction between a dislocation and impurities in KCl single crystals. *J. Mater. Sci.* **1993**, *28*, 6329–6332. [[CrossRef](#)]
88. Johnston, W.G. Effect of impurities on the flow stress of LiF crystals. *J. Appl. Phys.* **1962**, *33*, 2050–2058. [[CrossRef](#)]
89. Gaiduchenya, V.F.; Blistanov, A.A.; Shaskol'skaya, M.P. Thermally activated slip in LiF crystals. *Sov. Phys. Solid State* **1970**, *12*, 27–31.
90. Kohzuki, Y. Study on the interaction between a dislocation and impurities in KCl:Sr²⁺ single crystals by the Blaha effect part I Interaction between a dislocation and an impurity for the Fleischer's model taking account of the Friedel relation. *J. Mater. Sci.* **2000**, *35*, 3397–3401. [[CrossRef](#)]
91. Kohzuki, Y.; Ohgaku, T. Study on the interaction between a dislocation and impurities in KCl:Sr²⁺ single crystals by the Blaha effect Part II Interaction between a dislocation and aggregates for various force-distance relations between a dislocation and an impurity. *J. Mater. Sci.* **2001**, *36*, 923–928. [[CrossRef](#)]
92. Sprackling, M.T. Three-stage Hardening. In *The Plastic Deformation of Simple Ionic Crystals*; Alper, A.M., Margrave, J.L., Nowick, A.S., Eds.; Academic Press: London, UK, 1976; pp. 203–206.
93. Alden, T.H. Latent hardening and the role of oblique slip in the strain hardening of rock-salt structure crystals. *Trans. Met. Soc. AIME* **1964**, *230*, 649–656.
94. Davis, L.A.; Gordon, R.B. Plastic deformation of alkali halide crystals at high pressure: Work-hardening effects. *J. Appl. Phys.* **1969**, *40*, 4507–4513. [[CrossRef](#)]
95. Evans, A.G.; Pratt, P.L. Work hardening in ionic crystals. *Philos. Mag.* **1970**, *21*, 951–970. [[CrossRef](#)]
96. Michalak, J.T. The influence of temperature on the development of long-range internal stress during the plastic deformation of high-purity iron. *Acta Metall.* **1965**, *13*, 213–222. [[CrossRef](#)]
97. Kohzuki, Y. Study on the interaction between a dislocation and impurities in KCl:Sr²⁺ single crystals by the blaha effect Part IV influence of heat treatment on dislocation density. *J. Mater. Sci.* **2009**, *44*, 379–384. [[CrossRef](#)]



© 2018 by the author. Licensee MDPI, Basel, Switzerland. This article is an open access article distributed under the terms and conditions of the Creative Commons Attribution (CC BY) license (<http://creativecommons.org/licenses/by/4.0/>).